THE JOURNAL OF PHYSICAL CHEMISTRY C
A JOURNAL OF THE AMERICAN CHEMICAL SOCIETY

pubs.acs.org/JPCC

Article

Chromophore Analysis of Near-Edge X-ray Absorption Spectra: Application to Four-Coordinate Phosphorus

Allan L. L. East,* M. Jake Pushie,* Nicole J.-Y. Zhang, and Brian T. Sterenberg*

Cite This: *J. Phys. Chem. C* 2024, 128, 14750−14760

Read Online

ACCESS | Metrics & More | Article Recommendations | Supporting Information

ABSTRACT: This paper reports *X-ray chromophore* behavior: the substituents of an X-ray-absorbing atom (here phosphorus) were found to contribute consistent absorptions, in intensity and in relative peak position (transition energy). Linear relations for absolute peak position, as a function of the sum of the phosphorus neighbor-atom electronegativities ($\Sigma\chi$), have been found for ten chromophore peaks: P−F, P−O, P−Cl, P−N, P−C_I, P−W_I, P−C_{II}(Ph), P−C_{II}(pyr) P−C_{II}(Fc), P−W_{II}. The discovery was made by finding (i) surprisingly rich phosphorus K-edge X-ray absorption spectra [P X-ray absorption spectroscopy (XAS)] for several four-coordinate-phosphorus compounds, including four new ones involving the $W(CO)_5$ substituent, (ii) a vastly improved time-dependent (linear-response-based) density-functional-theory prediction method for P XAS which provides unprecedented XAS peak-assignment ability, and (iii) a fresh antibonding-orbital-based interpretive framework. The discovery, that selective X-ray excitation of substituents is possible, opens the door for studies of chemical reactivity implications (X-ray photochemistry), and improved studies of X-ray radiation exposure effects and damage.

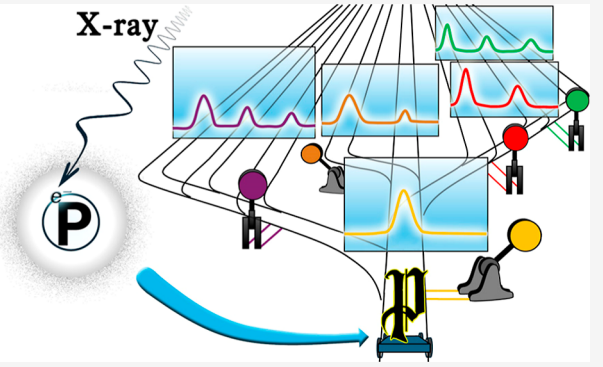

1. INTRODUCTION

Intense synchrotron X-ray sources revitalized the field of X-ray absorption spectroscopy (XAS) in the late 1970s.[1] Different types of fine structure provide different information about material structure around the absorbing atom whose electron is excited by X-rays: in EXAFS (extended X-ray absorption fine structure) it is the peaks (fine structure) at energies which may be hundreds of eV higher than the core-ionization edge, providing information on the structural positions of neighboring atoms,[1,2] while in NEXAFS or XANES (near-edge XAS) it is the peaks on or near the edge, providing information on electronic structure near the absorbing atom.[1,3−5] The near-edge XAS is also a sensitive chemical fingerprinting technique that can detect subtle differences in chemical speciation.[3,4] Near-edge XAS can be performed on a broad range of sample types, including powders, bulk solids, liquids and solutions,[5] and gases.[6,7]

Soft X-rays (below 3 keV) can excite K-shell (1s-orbital) electrons of third-row atoms (e.g., P, S, Cl), and synchrotron facilities offer an excellent source of tunable, high flux, X-rays for performing these experiments, even under ultradilute conditions. In particular, studies of the sulfur K-edge have demonstrated their utility, in metal−sulfur bond studies[8−12] or general organosulfur studies,[13−31] for example in differentiation of tautomeric structures.[14,16]

The current report focuses on phosphorus 1s near-edge XAS. After initial studies on phosphate and phosphite vapor spectra (P_4O_6, P_4O_{10}, $OP(OPh)_3$, SP_4O_6, ...)[32,33] one avenue of research pursued the small but reproducible differences among various mineral phosphates[34−38] and applications to detection in soils.[37,39−42] Such near-edge spectra possess a dominant white line for the 1s(P) → σ^*_{PO} orbital transition, whose position (transition energy) depends primarily on the P-oxidation state (phosphite vs phosphate), and smaller secondary near-edge absorptions, whose positions and intensities depend primarily on the counterion (Ca^{2+}, $Fe^{2+/3+}$, etc.). A different avenue of study concerned alternative phosphorus substituents (other than O), where more substantial changes to the spectra appear.[35,43−46] However, this phenomenon represents an untapped potential for spectral analysis due to lack of development of methodology for peak assignments. Daly and co-workers have made some significant progress with combined experiment-and-theory studies of several such compounds,[47−51] which helps set the stage for further development in this area.

We present P 1s near-edge XAS spectra for four substituted tungsten phosphines which particularly expose both this untapped potential and the need for better means of assigning

Received: June 11, 2024
Revised: July 31, 2024
Accepted: August 6, 2024
Published: August 21, 2024

https://doi.org/10.1021/acs.jpcc.4c03887
J. Phys. Chem. C 2024, 128, 14750−14760

peaks to transitions. Herein we compare experimentally obtained phosphorus K-edge XAS data with quantum chemistry-predicted spectra—with particular focus in four-coordinate phosphorus molecules and ions. A particular quantum-chemistry approximation was found of sufficient accuracy to allow both peak assignment in known spectra, and peak prediction in future spectra. This led to the discovery that phosphorus substituents contribute consistent absorptions, in intensity and in relative peak position (transition energy), and therefore could be regarded as behaving as X-ray chromophores. Some theoretical background is first reviewed.

1.1. Oscillator Strength. Absorption intensity (probability) is proportional to oscillator strength f, which is proportional to the square of the transition dipole moment $\langle\Psi_i|\vec{\mu}|\Psi_j\rangle$, where Ψ_i and Ψ_j are the initial and final electronic states of photoabsorption[52]

$$f_{ij} = \frac{8\pi^2 m_e c\tilde{\nu}_{ij}}{3he_0^2}|\langle\Psi_i|\vec{\mu}|\Psi_j\rangle|^2$$

Here, m_e, c, $\tilde{\nu}_{ij}$, h, and e_0 are respectively the electron mass, speed of light, wavenumber of the transition, Planck's constant, and electron charge. Oscillator strengths are quite small in XAS, compared to those observed in ultraviolet/visible spectroscopy, because the starting core orbital (here the P 1s) has poor wave function overlap with receiving (target) orbitals. Most of the predicted spectra herein show relatively constant total oscillator strengths (akin to a sum rule) from molecule to molecule: roughly $f = 0.02$, spread across an A band or set of bands, and another $f = 0.02$ spread across a B band or set of bands. We shall later argue that the origin of these intensities are, respectively, the 3p and 4p atomic orbitals of P, which contribute to several molecular orbitals (MOs).

1.2. Oxidation State Effects. A useful oxidation-state rule of thumb, worth reiterating here, states that core electrons become more strongly bound (therefore requiring higher excitation energies) as valence electrons are pulled farther away from the parent atom, i.e. as the atom's oxidation state is raised. In sulfur K-edge spectra the move from sulfide (S^{-II}) to sulfate (S^{+VI}) shifts the ionization edge up ~12 eV (from ~2470−2472 to 2482 eV, depending on the method of experimental energy calibration).[4] In phosphorus K-edge spectra Küper and Hormes showed that the move from elemental P (P^0) to phosphate (P^V) shifts the edge-obscuring "white line" peak up roughly 7 eV (from 2144.5 to 2152 eV, as reported),[53] while Yin et al.[35] showed that the move from phosphine ($Ph_2PCH_2PPh_2$) to phosphate resulted in a shift of +6 eV (from 2143 to 2149 eV, as reported—note that modern calibration places the phosphate white line peak closer to 2154 eV,[45,49] as opposed to the 2149−2150 eV values cited in some work). Indeed, X-ray excitation energies could well be used to define oxidation states for phosphorus, as it has been noted that the definition of oxidation state for phosphorus in some compounds is not always clear. As we shall demonstrate, the effect seems to be roughly +1 eV per oxidation step from −III to +V.

2. EXPERIMENTAL METHODS

The compounds $[W(CO)_5\{PPh_2(2\text{-}C_4H_5N)\}]$,[54] $[W(CO)_5(PCl_2N(CH_2CH_3)_2)]$,[55] and $[W(CO)_5(PPhCl_2)]$[56] were synthesized using published procedures. $[W(CO)_5(PPhFc_2)]$ (Fc = ferrocenyl) was synthesized from $[W(CO)_5(PPhCl_2)]$ by converting chloro to triflate using silver triflate, followed by electrophilic substitution with ferrocene. This sequence was repeated twice to form $[W(CO)_5(PPhFc_2)]$, using published methods.[57] The W-containing compounds were mounted as finely ground powders, with a thin layer of the powder placed on carbon tape and mounted in an electron yield apparatus with the front window and sample biased with 45 V. The total electron yield was measured by a pick-up grid. Additional phosphorus-containing standards, including the disodium salt of ATP and sodium phosphate, were prepared as 36 mM aqueous solutions at pH 7.0, buffered with 100 mM bis-Tris. The Mg^{2+}-ATP solution was prepared as 36 mM ATP and titrated to a final concentration of 100 mM Mg^{2+} using a concentrated stock solution of $Mg(NO_3)_{2(aq)}$. The X-ray absorption of solutions was monitored with a passivated implanted planar silicon detector (PIPS) to measure emitted X-ray fluorescence.

XAS data was collected at the Stanford Synchrotron Radiation Lightsource (SSRL) on bend magnet beamline 14-3, with the 3.0 GeV storage ring operating at 500 mA in top-up mode. The beamline used a Si(111) double crystal monochromator in the $\phi = 90°$ orientation to produce an unfocused beam 1 mm × 5 mm. This crystal at SSRL beamline 14−3 diffracts well at the desired energy range (2.14−2.19 keV), despite this being near the lower limit of what the monochromator can reach (nominal range 2.10−5.00 keV). Ionization chambers and the sample space employed $He_{(g)}$ and the sample space was allowed to purge for 15 min after each sample change until the measured $O_{2(g)}$ was below 0.7%. Prior to data collection the instrument dark currents were collected for 30s with the beam off to establish offsets for all detector readings. The monochromator energy was calibrated using solid tetraphenylphosphonium bromide (PPh_4Br) mounted to an upstream sample rod which could be lowered into the beam as-needed without breaking the $He_{(g)}$ atmosphere and its fluorescence intensity was measured with a photodiode. The peak of the white line of the PPh_4Br standard P K-edge spectrum was calibrated to 2146.96 eV[49] and was confirmed before each sample spectrum acquisition. P K-edge data was processed using EXAFSPAK (George, G. N.; http://www-ssrl.slac.stanford.edu/exafspak.html).

3. COMPUTATIONAL METHODS

All calculations were performed on the Graham supercomputer at Waterloo, Canada, managed by Canada's national Digitial Alliance consortium. Geometry optimizations were performed with Gaussian16 (rev C.01) software;[58] the ESM (electronic structure method of approximation) was B3LYP/6-31G(d) (compounds without tungsten) or B3LYP/SDD (compounds with tungsten).[58] Molecules having symmetry were optimized with point-group symmetry: $P(OMe)_4^+$, S_4; $PMe(OMe)_3^+$, C_1; $PMe_2(OMe)_2^+$, C_2; $PMe_3(OMe)^+$, C_s; PMe_4^+, T_d; PPh_4^+, S_4; $PO_4^{3-}\cdot 4H_2O$, D_{2d}; PCl_4^+, T_d; PF_4^+, T_d.

The spectra predictions were performed with single-point linear-response time-dependent density functional theory (TD-DFT)[59,60] with the default Tamm-Dancoff approximation[61] using the ORCA 5.0 software package.[62] The ESM used for these calculations was "BHANDHLYP CC-PVDZ ZORA NORI," which employs the hybrid DFT BH&HLYP,[63,64] the cc-pVDZ basis set,[65−67] and the Zero-Order Regular Approximation for relativistic effects,[68] while turning off ("NORI" flag) the default Resolution of Identity (density-fitting) approximation (RI)[69] for integrals. For all tungsten-

https://doi.org/10.1021/acs.jpcc.4c03887
J. Phys. Chem. C 2024, 128, 14750−14760

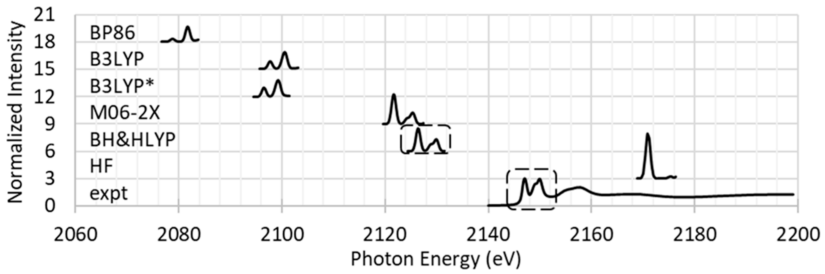

Figure 1. TD-DFT absorption spectra predictions for PPh_4^+, compared to experiment. Nonrelativistic calculations, cc-pVDZ basis set (except the asterisked case where the alternative def2TZVP basis set was used to demonstrate the minor basis set effect). Intensities obtained by applying 1 eV Gaussian line broadening and scaling by 1/100 to mimic edge-normalized spectra from experiment. The % Hartree−Fock exchange in the DFT approximations are 0 (BP86), 20 (B3LYP), 57 (M06-2X), 50 (BH&HLYP), and 100 (HF); see Supporting Information for references and further tests. Circled choice (BH&HLYP) showed best agreement with experiment.

containing molecules, the basis set SARC-ZORA-TZVP[70] was used for the W atom, using the "% basis" setting. Quadrupole contributions to oscillator strengths[71] were included, using "DoQuad true", though this gave negligible effects to the dipole-dominated spectra. Intensities in the predicted spectra presented herein were computed from ORCA-computed oscillator strengths by using Avogadro 1.2.0 software (http://avogadro.cc/)[72] and applying 1 eV Gaussian line widths to each of the ORCA-calculated oscillator strengths, then scaling these by 1/100.

The ESM described above was selected after testing (see Supporting Information). Some important theoretical findings are worthy of note here. Absolute peak position (excitation energies) are most sensitive to the P 1s core orbital energy, and for this, (i) the cc-pVDZ basis set was one of many that gave sufficient description of the P 1s orbital, and (ii) of the two approximations for relativistic corrections tested, these generally shifted all peaks (the entirety of the predicted spectrum) to higher energy by 6−7 eV and 12−14 eV, respectively, due to lowering the P 1s orbital energy. The larger ZORA correction was chosen merely because it reduced the error in the absolute peak position prediction (specifically on the test peak, the 2147 eV peak in the PPh_4^+ spectrum) from −19 to −7 eV, once the DFT method (BH&HLYP) was chosen. The choice of BH&HLYP, over other DFT methods, such as BP86 used by DeBeer and co-workers,[12,71,73] and B3LYP used by Daly and co-workers,[26,49,51] was made for both absolute peak position and relative peak intensity justifications (Figure 1).

Anions, like PO_4^{3-} and the condensed phosphates $O(PO_3)_x^{-2-x}$, posed specific computational modeling challenges. Use of the cc-pVDZ basis set yields a poor description of the diffuse σ^*_{P-O} target orbitals, and though diffuse functions could be supplemented in the calculation (e.g. aug-cc-pVDZ), these result in the addition of unrealistic Rydberg states in the single-molecule ("gas-phase") calculation. Rydberg states do not appear in condensed-phase systems. Hence, for PO_4^{3-}, cc-pVDZ was kept but explicit water molecules were added to the compution ($PO_4^{3-}\cdot 4H_2O$, both DFT geometry optimization and TD-DFT spectra prediction); this provides more realism and contributes additional basis functions to the system, which ultimately improves the σ^*_{P-O} orbital description. Only monophosphate was included in this work (see Supporting Information for water placement); a follow-up study of condensed phosphates is planned.

4. EXPERIMENTAL RESULTS

Figure 2 presents our synchrotron-measured spectra. We designate the band groups A, B, and C for ease of discussion.

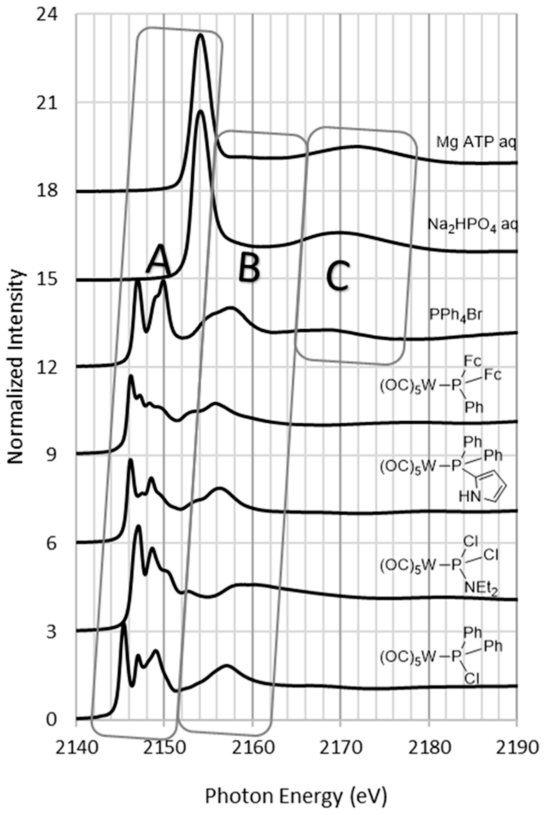

Figure 2. Synchrotron XAS spectra in the phosphorus K-edge region for seven phosphorus compounds, with band classification. Spectra normalized to have an ionization edge of intensity 1. The C band is an EXAFS photoelectron backscattering amplitude.

The phosphate spectra (top 2 traces) are quite similar to spectra obtained by others,[34−39,45] and show the well-known A band ("white line") at 2154 eV and a broad "C" band at 2166−2178 eV. This C band was assigned by Dalba et al.[74] to the extended (EXAFS) region: the first four P K-edge EXAFS amplitudes (C, D, E, and F bands) must be centered at 17, 88, 210, and 380 eV beyond the core ionization threshold, to correspond to published EXAFS spectra[74,75] which show amplitude maxima at photoelectron wave numbers k of 2.1, 4.8, 7.4, and 10.0 radians per Å. These EXAFS amplitudes are

https://doi.org/10.1021/acs.jpcc.4c03887
J. Phys. Chem. C 2024, 128, 14750−14760

caused by backscattering interference with the out-going photoelectron, arising from the phosphate oxygen atoms, which backscatter at distance R = 1.2 Å from the origin of the P 1s electron; the Fourier transform of R = 1.2 Å gives the EXAFS oscillation $\sin(2kR + \pi)$, with maxima when k satisfies $2kR + \pi = \pi/2 + 2\pi n$, n = 1, 2, and so on.

In contrast, the nonphosphate spectra (Figure 2 left, lower 5 traces) show a more exciting A band with subpeaks (2144−2152 eV), and an unexpected and substantial broad B band (2152−2162 eV) not seen in the phosphate spectra (except perhaps a hint of one in the ATP spectrum). In the case of highly symmetric PPh_4^+ there is also a broad C band (2164−2174 eV) that is likely to be an EXAFS oscillation amplitude, as with the phosphates. B bands can be seen in other known P K-edge spectra,[43,44,49,53] and A-band subpeaks have been seen as well.[43,44,47−51]

Assignments of the bands and subpeaks in the presented spectra (Figure 2) are made in the next section.

5. COMPUTATIONAL RESULTS

5.1. P^+, PMe_4^+, and PPh_4^+. The S_4-symmetry BH&HLYP TD-DFT predicted spectrum of PPh^+_4 (3rd trace, Figure 3)

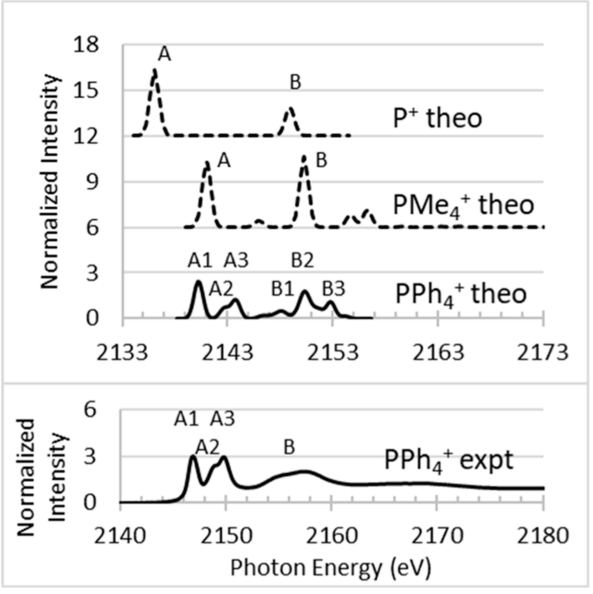

Figure 3. TD-DFT (theo) spectra (with applied 1 eV Gaussian line widths) for P^+, PMe_4^+, and PPh_4^+, and the experimental spectrum of PPh_4^+ from Figure 2. The P^+ spectrum was run with aug-cc-pVDZ basis set and unrestricted orbitals from a quintet (^5S) ground state, showing only β-electron excitations; its A and B bands are from 1s → 3p and 1s → 4p excitation.

agrees even better with the experimental data (4th trace) than the earlier D_{2d}-symmetry B3LYP TD-DFT spectrum of the A band,[49] which had done well with relative subpeak position but not relative subpeak intensities. Operating with the assumption that the states causing each theoretical peak are the ones causing the corresponding experimental peak, the task then is to interpret the corresponding upper-state wave functions causing each peak in the TD-DFT calculations, to qualitatively assign the peaks to transitions.

Since the A and B bands of bare P^+ ion are clearly due to 1s → 3p and 1s → 4p transitions, we use Figure 3 to argue that the A and B bands of any P K-edge XAS are excitations to MOs that likely contain phosphorus 3p and phosphorus 4p contributions, respectively. Further support comes from the visual comparison of chromophoric A and B band target MOs of PMe_4^+ to those of P^+ (Figure 4). The B-A energy gap is seen

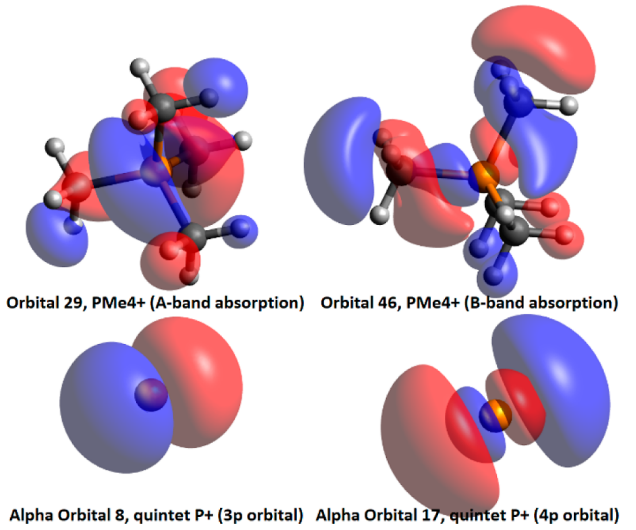

Figure 4. Kohn−Sham target (unoccupied) orbitals from BH&HLYP calculations of ground-state PMe_4^+ and unrestricted-orbital quintet[5]-state P^+ atomic ion, attempting to show the similarity of an A-band orbital (upper left) to phosphorus 3p (lower left) and a B-band orbital (upper right) to phosphorus 4p (lower right). Both the 3p and 4p target orbitals produce intensity in a TD-DFT P K-edge XAS calculation on quintet-state P^+ (Figure 2).

to be 13 eV for atomic P^+ and 10 eV for molecular P^+; the smaller value for molecular P^+ is due to the raising of the 3p orbital energy due to antibonding (σ^*_{P-C}) combination with a substituent orbital.

The intensity of the B band in Figure 3 is interesting, in two aspects. First, in the experimental spectrum it is considerably broadened, compared to A band intensity. One possible reason is autoionization-lifetime[76,77] broadening: these states are roughly 8 eV above the core-ionization threshold, shortening the upper-state lifetime (with regards to spontaneously ionizing). Another possible reason is nearest-neighbor broadening: the 4p orbital of P (relevant to the B band) may be sufficiently large as to interact with neighboring molecules, present in the solid-state experimental spectra but not in the computed one. This would make B-band transitions sensitive to intermolecular distances, which have wider thermal distributions than intramolecular distances. Pettersson and co-workers have considered nearest-neighbor broadening effects to explain the A-band broadening in oxygen K-edge XAS spectra of water and ice, vis-a-vis water vapor.[78]

The second interesting aspect about B-band intensity here is that it is surprisingly nearly equal to the A-band intensity, in PPh_4^+ and in PMe_4^+. This is not so for P^+, whose predicted spectrum shows a halving of intensity in going from the 1s → 3p to the 1s → 4p transition. To probe why, we first checked for possible inaccuracies in the TD-DFT spectra by trying alternative basis sets. The B bands intensities showed more sensitivity to such changes than the A bands, reflecting greater uncertainty in the predicted B band intensities. (Of note, augmentation of basis sets with more and more diffuse functions had the effect of introducing more continuum ionization states, taking intensity away from the B band.) So as

https://doi.org/10.1021/acs.jpcc.4c03887
J. Phys. Chem. C 2024, 128, 14750−14760

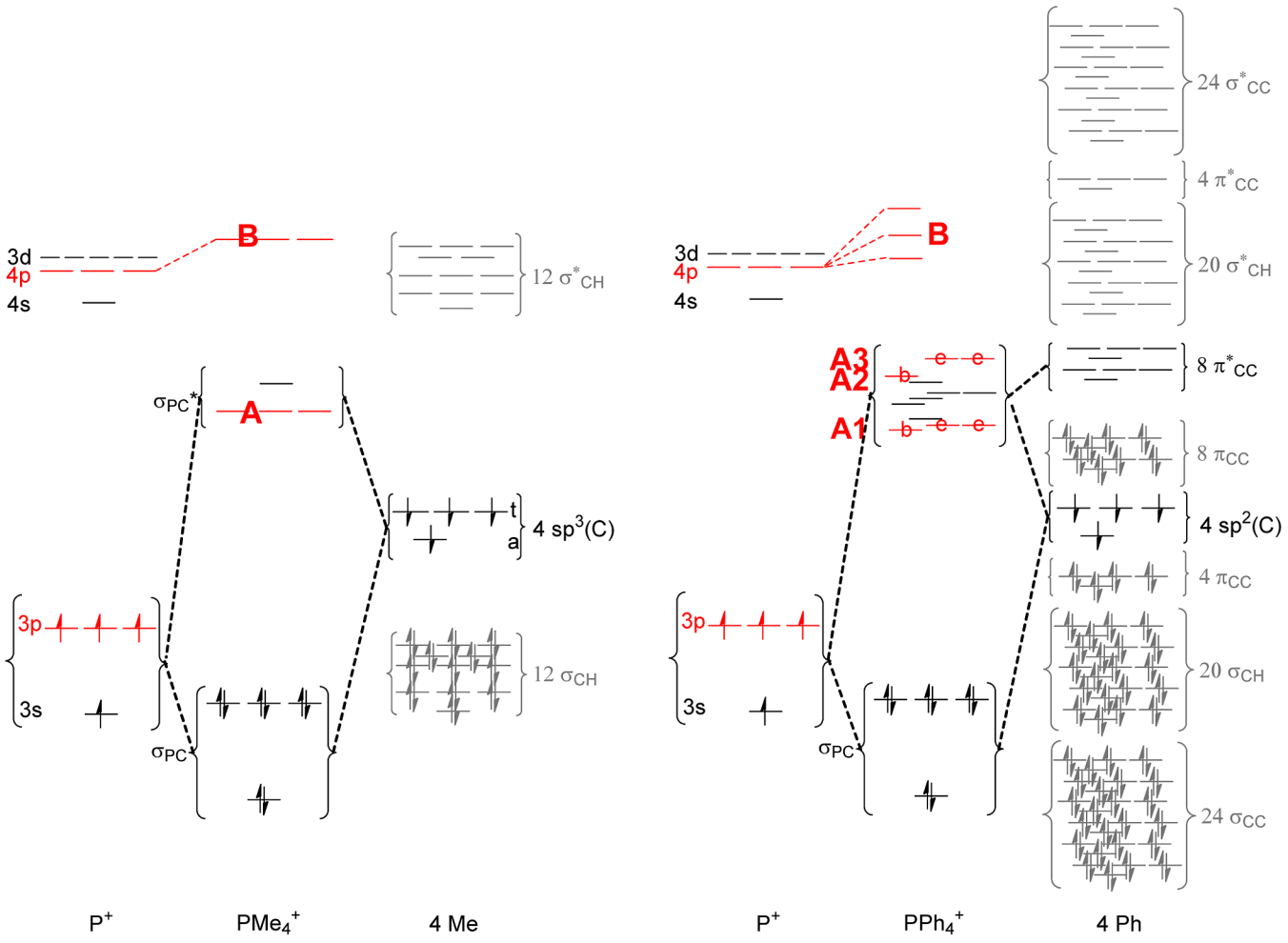

Figure 5. Two orbital energy-level mixing diagrams (PMe_4^+ at left, PPh_4^+ at right), to explain the origin of the intensity of the A and B XAS bands, and the origin of the first-order splitting of the A band in the case of PPh_4^+. Orbital energy level spacings are simplified but are based on DFT (BH&HLYP/cc-pVDZ) orbital energies, and for this (i) the DFT runs for P^+, 4 Me, and 4 Ph were performed as quintet states with unrestricted orbitals, (ii) the alpha- and beta-electron versions of each orbital energy were later averaged, and (iii) the 4 Me and 4 Ph quintet runs were performed by using the geometry of the parent phosphonium ion and removing the P^+ from the calculation.

a further check on the TD-DFT P^+ spectrum, hand derivation of expected oscillator strengths (see Introduction) for the 1s → *np* transitions of P^+ atomic ion were performed, using a one-electron model, assuming Z_{eff} values from Slater's Rules and the energy level expression $E_n = -(Z_{eff}^2/n^2)$ Ry, (Ry = Rydberg energy constant = 13.6057 eV). The lengthy derivations are presented in Supporting Information The results for $\{f_{13}, f_{14}, f_{15}, f_{16}\}$ to the {3p, 4p, 5p, 6p} states are $\{0.015, 4 \times 10^{-4}, 6 \times 10^{-6}, 4 \times 10^{-6}\}$ respectively. The 0.015 value matches very well the 0.02 sum of A-band oscillator strength in the TD-DFT computations, not just for P^+ but any of our molecular species containing one P atom. In contrast, the 4×10^{-4} value for the B band is considerably lower than the TD-DFT value (0.007, from BH&HLYP/aug-cc-pVDZ), possibly due to better consideration of continuum-state intensities (see Fano and Cooper[79] Section 5.2). Though the two calculations disagree on the P^+ B/A intensity ratio, they both agree that the ratio is less than one, unlike what is seen in the spectra of PMe^+ and PPh_4^+ (and the four $W(CO)_5$-containing species, Figure 2). Hence the phenomenon of enhanced B-band intensity, when P^+ is in a molecule, seems real. Our proposed explanation is that this enhanced B-band intensity is due to intensity borrowing from continuum states equal in energy, caused by the phosphorus substituents which introduce more localized state possibilities.

Moving on to peak assignment, in the case of PMe_4^+ (a P–C_{alkyl} case), the TD-DFT spectrum (2nd trace in Figure 3) predicts a single A-band peak (f = 0.016), to a degenerate *t*-symmetry P(3p) σ^*_{P-C} trio of MOs, and a single B-band peak (f = 0.017), to a degenerate *t*-symmetry methyl-perturbed-P(4p) trio of MOs (Figure 5). The A-band degenerate trio arises from three spectroscopically allowed (*t*-symmetry) linear combinations of the four expected σ^*_{P-C} orbitals; the fourth combination is a spectroscopically forbidden *a*-symmetry orbital. On either side of the predicted B band of PMe_4^+ (second trace of Figure 3) are three minor peaks, that result from intensity borrowing by "dark" states, i.e. mixing with additional unoccupied *t*-symmetry orbitals on the substituents (e.g. the 12 σ^*_{C-H}) that were expected to have such poor overlap with 1s(P) as to provide no intensity on their own. Lifetime broadening should render these minor peaks to be experimentally inconsequential.

In the case of PPh_4^+ (a P–C_{aryl} case), third and fourth traces in Figure 3, both the A and B bands are further split. We focus on the A subpeaks (A1, A2, and A3, at 2147, 2149, and 2150 eV), which have been reproduced in the TD-DFT predicted

https://doi.org/10.1021/acs.jpcc.4c03887
J. Phys. Chem. C 2024, 128, 14750−14760

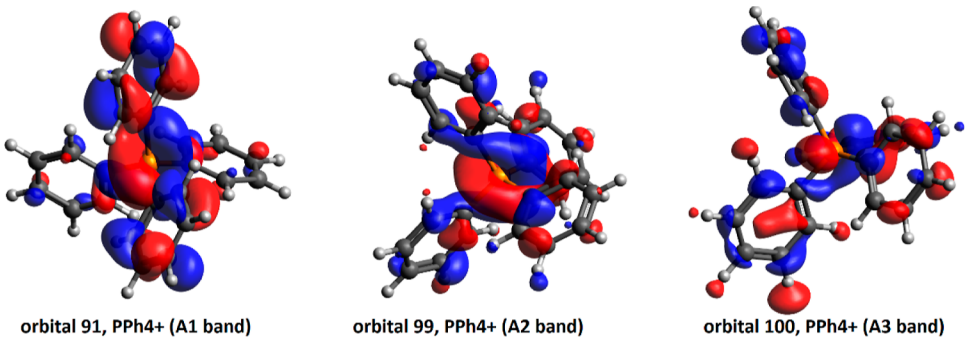

Figure 6. Examples of the destination orbitals of the A1, A2, and A3 bands of PPh_4^+. Note in particular the interaction of the P 3p with aryl π^*_{C-C} phenyl orbitals in orbital 91 (A1 subpeak).

spectrum. There is a first-order splitting of almost 3 eV, separating A1 (f = 0.009) from A2+A3 (the remaining f = 0.006), due to strong mixing of the P 3p orbital with not one but two orbitals on the aryl carbon: the usual sp^2 or sp^3 hybrid orbital (in an antibonding manner), causing one σ^*_{P-X} target MO per Ph group, and an extra "aryl" one, a delocalized π^*_{C-C} orbital (in a bonding manner), causing one $3p_P + \pi^*_{C-C}$ target MO per Ph group. Due to reduced (S_4) symmetry compared to PMe_4^+, linear combinations of the four $3p_P + \pi^*_{C-C}$ MOs result in (a,b,e,e) symmetry orbitals, with the (b,e,e) trio the optically allowed ones (MOs 90−92; the A1 subpeak). The same (a,b,e,e) symmetry breakdown occurs with the four σ^*_{P-X} MOs, providing another optically active trio (MOs 99−101; the A2 and A3 subpeaks). This is shown diagrammatically in Figure 5. The separation of the A2 band (f = 0.002) from the A3 band (f = 0.004) is a second-order splitting of almost 1 eV, allowed by the b/e symmetry difference; in this trio the b-symmetry state (with MO 99) is surprisingly significantly energetically preferred over the e-symmetry states. Within the A2 band, there is even a third-order splitting of only 0.3 eV in the TD-DFT calculation, imperceptible in spectra with 1 eV line broadening, caused by an electronic resonance of the anomalously low b-symmetry σ^*_{P-C}-occupied state with a "dark" b-symmetry π^*_{C-C} state, causing mixing and the minor splitting. Examples of the TD-DFT destination MOs for these A1, A2, and A3 bands appear in Figure 6.

5.2. Oxidation Series $P(OMe)_nMe_{4-n}^+$ (n = 0,1,2,3,4). To probe the oxidation state effect, Figure 7 shows the TD-DFT predicted spectra of the series $P(OMe)_nMe_{4-n}^+$, n = 0−4.

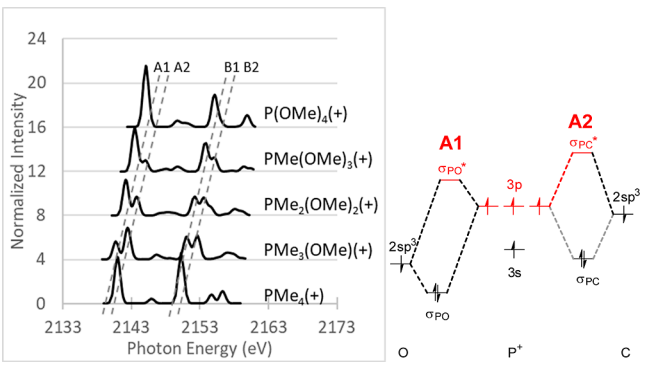

Figure 7. Left: TD-DFT predicted spectra for the oxidation series $P(OMe)_nMe_{4-n}^+$, n = 0−4. Experimental spectra would be expected to be shifted +7 eV with considerably broadened B-band peaks (see Figure 3). Right: orbital energy mixing diagram, showing the origin of the A-band splitting.

Again we see A and B bands, but with further splitting due to mixed substituents: separation of the energies of MOs in the P−O direction from those in the P−C direction. Hence the {A1, A2, B1, B2} peaks are assigned as {σ^*_{P-O}(3p), σ^*_{P-C}(3p), P(4p)-O, P(4p)-C} respectively.

All four peaks shift to higher energy with increasing oxidation (replacement of each Me by OMe) by an amount 1.4n eV, where n is the number of replacements. Of this 1.4n eV, roughly two-thirds results from the lowering of the P 1s orbital energy (which drops from from −2148.6 eV in PMe_4^+ to −2151.9 eV in $P(OMe)_4^+$). The remaining one-third is due largely to the rise of the σ^* orbital energies, plus correlation effects in producing state energies from orbital energies. The rise of this antibonding orbital energy can be directly related to the shrinking P−O distance in this oxidation series; such an effect was demonstrated in carbon K-edge XAS fourty years ago.[80] The net oxidation shift of 1.4n eV, on the transition energy, is slightly larger for the A1 peak (1.45n) than the A2 peak (1.35n), due to σ^*_{P-O}(3p) rising faster than σ^*_{P-C}(3p) does. This observed difference in shift rate among A-band subpeaks will be incorporated into predictive equations for subpeak locations (section 5.4).

5.3. Four Tungsten Complexes. Figure 8 shows the TD-DFT predictions for the four tungsten-complex spectra we obtained experimentally (Figure 2, dashed curves in Figure 8). Individual state lines are shown, inside the 1 eV-broadened spectra. We have analyzed the wave functions of the underlying states, to make peak assignments. The A-band region is 2144−2154 eV. The first A subpeak in the upper two plots is the "Cl peak," containing the transition(s) 1s(P) → σ^*_{P-Cl}, one for each P−Cl bond in the molecule. The first A subpeak in the lower two plots is the "first carbon peak" or "C_I peak," one per P−C bond. Aryl-carbon substituents (Ph, Fc, pyrrole) contribute not 1 but 2 peaks to the spectrum at this 1 eV resolution, according to the predictions. This C_I peak also appears in the second spectrum, at 2147 eV experimentally. The −7 eV error made on C_I is consistent in this sample of spectra, as can be seen in Figure 8 where all TD-DFT spectra have been shifted +7.0 eV to line up these peaks with experiment. One can see that the Cl peak prediction is still misaligned, but consistently so in the upper two spectra, seemingly in error by −8.5 eV instead of −7.0 eV. The consistency of this error made on each type of peak greatly aided analysis. We exploited this in the next section with more predicted spectra, to help understand not only the remaining A subpeaks in Figure 8, but to spot trends with the electron-withdrawing power of substituents and to allow derivation of peak prediction formulas.

https://doi.org/10.1021/acs.jpcc.4c03887
J. Phys. Chem. C 2024, 128, 14750−14760

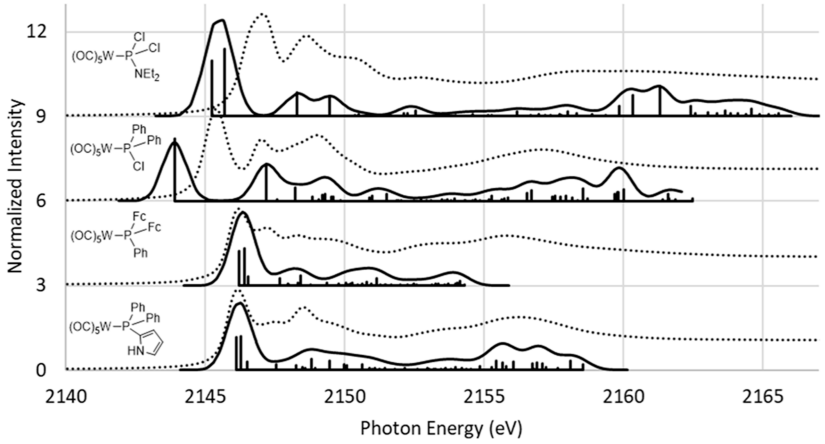

Figure 8. TD-DFT predicted spectra (presented at two different energy resolutions) for four compounds containing $W^0(CO)_5$ as a substituent of the absorbing phosphorus center. Ph = phenyl, Fc = ferrocenyl. The 2144−2154 eV and 2154−2164 eV regions are A-band and B-band in Figure 2. Dotted curves represent experimental data. TD-DFT spectra were shifted +7.0 eV to align with the first of the phenyl peaks in the experimental data: 2147 eV in $W^0(CO)_5PPh_2Cl$, 2146 eV in $W^0(CO)_5PPhFc_2$ and $W^0(CO)_5PPh_2Py$ (Py = pyrrole). The Cl peak (2144−2145.5 eV with TD-DFT) appears to require a different systematic shift (+8.5 eV) to match experiment.

5.4. Peak Positions Explained. The TD-DFT spectra of additional single-phosphorus molecules were obtained, resulting in a total of 26 molecules and 146 assigned subpeaks in the A bands of these spectra. It was found that each substituent produced consistent chromophoric *absorption(s)*, here labeled with index j, with comparable intensities, regardless of the other 3 substituents present, except for perturbations caused by occasional coincidental electronic resonances. The *locations* ΔE_{ij} of these peaks, however, did depend on the other 3 substituents present, as in Figure 7. We hypothesized that the locations ΔE_{ij} of each peak j might depend linearly on a single-variable oxidation-related property o_i of the molecule i

$$\Delta E_{ij} = m_j o_i + b_j$$

Such equations should find value for predicting and interpreting future spectra. To confirm the hypothesis, the peak locations in these 26 TD-DFT spectra were used to successfully determine 10 such relations (10 "lines"), for 10 chromophoric peak types j, designated F, Cl, O, N, C_I, W_I, Ph_{II}, Py_{II}, Fc_{II}, W_{II}. The electronically saturated substituents {F, Cl, O^- or OR, NR_2, R} give rise to single peaks, designated {F, Cl, O, N, C_I} with oscillator strength f_{osc} roughly {0.007, 0.006, 0.006, 0.005, 0.004} respectively. The electronically unsaturated substituents in this study gave rise to 2 peaks (at 1 eV resolution): for Ph, C_I (f_{osc} = 0.003) and Ph_{II} (0.001); for Py, C_I (0.003) and Py_{II} (0.001); for Fc, C_I (0.003) and Fc_{II} (0.001); and for $W(CO)_5$, W_I (0.002) and W_{II} (0.001).

Four possibilities for the property o_i were tested: the P 1s orbital energy in the molecule, the P partial charge (from Weinhold natural population analysis definition[81]), and the sum of electronegativities ($\Sigma\chi$) of the four neighboring atoms from two different scales (Pauling,[82] and Allen[83]). Visibly, the $\Sigma\chi$ choice was performing better, and the first-pass 20-parameter least-squares regression fits with these two definitions (Pauling $\Sigma\chi$ and Allen $\Sigma\chi$) gave rms errors of 0.56 and 0.59 eV, respectively, for 146 points covering a 12 eV range. Furthermore, an electronegativity definition of o_i would offer a much faster predictive method for the user, who would otherwise need a means of predicting the 1s orbital energy or the partial charge of P in their molecule. Upon examination of the fitted lines, we noticed that the Pauling and Allen scales differed considerably on their values for Cl and W. We therefore performed a third fit, in which we reoptimized the electronegativity values of 4 atoms (O, F, Cl, W, leaving C and N values anchored). This 24-parameter fit resulted in a significant reduction of rms error to 0.36 eV.

There is some uncertainty in the fitted slopes ("oxidative shift rates") m_j. There was, however, a visible trend in the lines from the 24-parameter fit: higher slopes for substituents having higher electronegativity. A total of 10 parameters could be eliminated from the fit if a two-parameter convergence point $\{o_{max}, \Delta E_{max}\}$ for all lines was imagined

$$\Delta E_{ij} = \Delta E_{max} - m_j(o_{max} - o_i)$$

This became our fourth and final fit of the 146 TD-DFT points (16 parameters: χ(O), χ(F), χ(Cl), χ(W), 10 slopes m_i, and o_{max} and ΔE_{max}, rms error 0.38 eV). The resulting electronegativities of best fit appear in Table 1, and other parameter values in Table 2. Figure 9 shows the fit lines atop the 26 TD-DFT spectra. The point $\{o_{max}, \Delta E_{max}\}$ from the fit is (35.3, 2174.75 eV). We have, as yet, no theoretical justification for the existence of a convergence point. At the moment it is merely a means of reducing dimensionality of fit without erasing the phenomenon of peak-dependent "oxidation-shift rates" observed in the TD-DFT data. An alternative 15-parameter fit, in which a common slope for all peak types was assumed (one m_j, ten independent b_j, four electronegativities), gave a demonstrably worse fit, rms error 0.44 eV.

Finally, what remained was to adjust the parameter values $\{o_{max}, \Delta E_{max}, 10\ m_j\}$ to reproduce experimental spectra instead

Table 1. Electronegativities for P Substituents

substituent atom	Pauling[82]	Allen[83]	optimal for P K-edge XAS
F	3.98	4.19	4.11
O	3.44	3.61	3.58
Cl	3.16	2.87	3.29
N	3.04	3.07	3.04[a]
C	2.55	2.54	2.55[a]
W	2.36	1.47	1.23

[a]Values fixed to those of Pauling during reoptimization.

https://doi.org/10.1021/acs.jpcc.4c03887
J. Phys. Chem. C 2024, 128, 14750−14760

Table 2. P K-Edge XAS (A-Band) Spectral Parameters for $\Delta E_{ij} = \Delta E_{max} - m_j\{(\Sigma\chi)_{max} - (\Sigma\chi)_i\}$[a]

parameter	TD-DFT	expt	full equation, expt
m_F	1.49		
m_O	1.42	1.35	$1.35(\Sigma\chi)_i + 2134.8$
m_{Cl}	1.48	1.47	$1.47(\Sigma\chi)_i + 2131.0$
m_N	1.37	1.39	$1.39(\Sigma\chi)_i + 2133.5$
m_{C_i}	1.35	1.38	$1.38(\Sigma\chi)_i + 2133.8$
m_{WI}	1.30	1.32	$1.32(\Sigma\chi)_i + 2135.6$
m_{PhII}	1.26	1.28	$1.28(\Sigma\chi)_i + 2136.9$
m_{pyrII}	1.23	1.27	$1.27(\Sigma\chi)_i + 2137.2$
m_{FcII}	1.22	1.24	$1.24(\Sigma\chi)_i + 2138.3$
m_{WII}	1.19	1.22	$1.22(\Sigma\chi)_i + 2138.8$
$(\Sigma\chi)_{max}$	35.33	31.73	
$(\Delta E)_{max}$ (eV)	2174.75	2177.57	

[a]Assume use of "optimal" electronegativities in Table 1.

of TD-DFT ones. This was done by refitting to the 7 spectra of Figure 2, keeping the electronegativities from our fourth TD-DFT peak fit, and the resulting parameter values also appear in Table 1 (rms error 0.22 eV). Future work should aim at adding to Tables 1 and 2, for other P substituents, and then to extend the idea to other K-edge XAS spectra (S, Cl, etc.).

6. CONCLUSIONS

Experimentally, it has been shown that the "white line" of four-coordinate phosphorus compounds in P K-edge XAS spectra (here identified as the A band) becomes split and produces subpeaks when a mix of substituents (P−O, P−C, P−W, etc.) are present. The chromophoric source of the A band is the 1s → 3p atomic transition, contributing to unoccupied σ^*_{P-X} MOs. In addition, a B band, not seen in the phosphate spectra, appears in the neutral and cationic four-coordinate phosphorus compounds. The considerable line broadening seen in the B band could be due either to very short preionization lifetime of the upper state, or greater variation in upper-state energy due to thermal variation of neighboring-molecule distances from the absorbing P atom. Evidence was provided to support our hypothesis that the chromophoric source of the B band is the 1s → 4p atomic transition, and since this intensity is predicted to be much smaller for P^+ atomic ion, it is argued that the molecules are borrowing intensity from the ionization continuum to produce their B bands by providing additional localized resonance states (with σ^* and π^* orbitals) at that energy. The B band does not appear in the experimental phosphate spectra (though it does appear in our TD-DFT spectrum of D_{2d}-symmetry $PO_4^{3-}\cdot 4H_2O$); this could be due to one of several possibilities, from extreme lifetime broadening (zero lifetime) for these states in anions, to extreme nearest-neighbor broadening due to the aqueous state, to something treated poorly by our modeling protocol.

Theoretical work found a predictive DFT method (BH&HLYP) which ably reproduces, using a TD-DFT excited-state algorithm, the measured XAS relative peak intensities, allowing for more reliable peak assignment of the experimental spectra, and demonstrating linear oxidative shift effects on these peak locations (Figure 7). Electronically unsaturated substituents (e.g., phenyl, ferrocenyl, $W^0(CO)_5$, etc.) provide more than one absorption peak, due to the introduction of an additional "aryl" π^*_{C-C} orbital possibility near enough to the P atom to perform intensity splitting with σ^*_{P-C}. Pencil-and-paper predictive eqs (Table 2) were

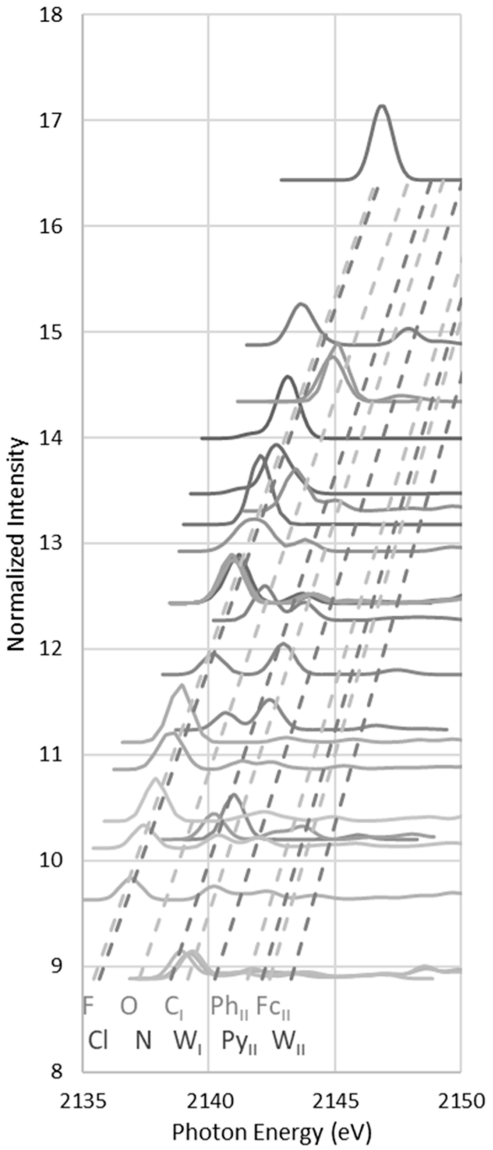

Figure 9. TD-DFT predicted spectra (with applied 1 eV line broadening) of 26 P-containing molecules (see Supporting Information for the list). Each spectrum was vertically shifted by the $\Sigma\chi$ value of the molecule. The 10 dashed lines are the Table 2 TD-DFT fitting lines, highlighting peak location dependence upon $\Sigma\chi$.

presented, for absolute peak locations as linear functions of a molecular property ($\Sigma\chi$) related to the phosphorus oxidation state; one set for BH&HLYP TD-DFT peak locations (e.g., Figure 9), and another for experimental peak locations (e.g., Figure 2).

Future work is planned to (i) test the broad applicability of these equations with measured spectra of an expanded range of phosphorus and poly phosphorus compounds, and (ii) to examine the subtle differences in band shape among phosphates, including "condensed" phosphates such as pyrophosphate, ADP, ATP, etc. which are commonly encountered in biological systems.

■ ASSOCIATED CONTENT

Supporting Information

The Supporting Information is available free of charge at https://pubs.acs.org/doi/10.1021/acs.jpcc.4c03887.

https://doi.org/10.1021/acs.jpcc.4c03887
J. Phys. Chem. C 2024, 128, 14750−14760

Contains pictures, Cartesian coordinates, and $\Sigma\chi$ values of the 26 molecules of Figure 9, more ESM test results, and derivation of atomic oscillator strengths for Section 5.1 (PDF)

AUTHOR INFORMATION

Corresponding Authors

Allan L. L. East − *Department of Chemistry and Biochemistry, University of Regina, Regina, Saskatchewan S4S0A2, Canada;* orcid.org/0000-0003-1898-4370; Email: allan.east@uregina.ca

M. Jake Pushie − *Department of Surgery, University of Saskatchewan, Saskatoon, Saskatchewan S7N5E5, Canada;* orcid.org/0000-0001-7494-5427; Email: jake.pushie@usask.ca

Brian T. Sterenberg − *Department of Chemistry and Biochemistry, University of Regina, Regina, Saskatchewan S4S0A2, Canada;* orcid.org/0000-0001-5579-4184; Email: brian.sterenberg@uregina.ca

Author

Nicole J.-Y. Zhang − *Department of Chemistry and Biochemistry, University of Regina, Regina, Saskatchewan S4S0A2, Canada*

Complete contact information is available at: https://pubs.acs.org/10.1021/acs.jpcc.4c03887

Notes

The authors declare no competing financial interest.

ACKNOWLEDGMENTS

Computational resources provided by Compute Ontario (computeontario.ca) and the Digital Research Alliance of Canada (alliance can.ca). Use of the Stanford Synchrotron Radiation Lightsource, SLAC National Accelerator Laboratory, is supported by the U.S. Department of Energy, Office of Science, Office of Basic Energy Sciences under Contract no. DE-AC02-76SF00515. The SSRL Structural Molecular Biology Program is supported by the DOE Office of Biological and Environmental Research, and by the National Institutes of Health, National Institute of General Medical Sciences (P30GM133894). The contents of this publication are solely the responsibility of the authors and do not necessarily represent the official views of NIGMS or NIH. The National Science and Engineering Research Council is acknowledged for funding: grants 2021-02522 (B.T.S.) and 2017-06247 (A.L.L.E.). Adin Clark is thanked for partial charge calculations and assistance in data analysis and plotting. Hamdi Bumraiwha is thanked for providing samples of the tungsten phosphine complexes.

REFERENCES

(1) Cramer, S. P.; Hodgson, K. O. X-Ray Absorption Spectroscopy: A New Structural Method and Its Applications to Bioinorganic Chemistry. *Prog. Inorg. Chem.* **1979**, *25*, 1−39.

(2) Lee, P. A.; Citrin, P. H.; Eisenberger, P.; Kincaid, B. M. Extended x-ray absorption fine structure − its strengths and limitations as a structural tool. *Rev. Mod. Phys.* **1981**, *53*, 769−806.

(3) Chen, J. G. NEXAFS investigations of transition metal oxides, nitrides, carbides, sulfides and other interstitial compounds. *Surf. Sci. Rep.* **1997**, *30*, 1−152.

(4) Henderson, G. S.; de Groot, F. M. F.; Moulton, B. J. A. X-ray Absorption Near-Edge Structure (XANES) Spectroscopy. *Rev. Mineral. Geochem.* **2014**, *78*, 75−138.

(5) Smith, J. W.; Saykally, R. J. Soft X-ray Absorption Spectroscopy of Liquids and Solutions. *Chem. Rev.* **2017**, *117*, 13909−13934.

(6) Hitchcock, A. P.; Newbury, D. C.; Ishii, I.; Stöhr, J.; Horsley, J. A.; Redwing, R. D.; Johnson, A. L.; Sette, F. Carbon K-shell excitation of gaseous and condensed cyclic hydrocarbons: C_3H_6, C_4H_8, C_5H_8, C_5H_{10}, C_6H_{10}, C_6H_{12}, and C_8H_8. *J. Chem. Phys.* **1986**, *85*, 4849−4862.

(7) Urquhart, S. G.; Gillies, R. Rydberg−Valence Mixing in the Carbon 1s Near-Edge X-ray Absorption Fine Structure Spectra of Gaseous Alkanes. *J. Phys. Chem. A* **2005**, *109*, 2151−2159.

(8) Rose Williams, K.; Hedman, B.; Hodgson, K. O.; Solomon, E. I. Ligand K-edge X-ray absorption spectroscopic studies: metal-ligand covalency in transition metal tetrathiolates. *Inorg. Chim. Acta* **1997**, *263*, 315−321.

(9) Glaser, T.; Hedman, B.; Hodgson, K. O.; Solomon, E. I. Ligand K-Edge X-ray Absorption Spectroscopy: A Direct Probe of Ligand-Metal Covalency. *Acc. Chem. Res.* **2000**, *33*, 859−868.

(10) Solomon, E. I.; Hedman, B.; Hodgson, K. O.; Dey, A.; Szilagyi, R. K. Ligand K-edge X-ray absorption spectroscopy: covalency of ligand−metal bonds. *Chem. Rev.* **2005**, *249*, 97−129.

(11) Ha, Y.; Tenderholt, A. L.; Holm, R. H.; Hedman, B.; Hodgson, K. O.; Solomon, E. I. Sulfur K-Edge X-ray Absorption Spectroscopy and Density Functional Theory Calculations on Monooxo Mo^{IV} and Bisoxo Mo^{VI} Bisdithiolenes: Insights into the Mechanism of Oxo Transfer in Sulfite Oxidase and Its Relation to the Mechanism of DMSO Reductase. *J. Am. Chem. Soc.* **2014**, *136*, 9094−9105.

(12) Kowalska, J. K.; Hahn, A. W.; Albers, A.; Schiewer, C. E.; Bjornsson, R.; Lima, F. A.; Meyer, F.; DeBeer, S. X-Ray Absorption and Emission Spectroscopic Studies of $[L_2Fe_2S_2]^n$ Model Complexes: Implications for the Experimental Evaluation of Redox States in Iron−Sulfur Clusters. *Inorg. Chem.* **2016**, *55*, 4485.

(13) Pickering, I. J.; Prince, R. C.; Divers, T.; George, G. N. Sulfur K-edge X-ray absorption spectroscopy for determining the chemical speciation of sulfur in biological systems. *FEBS Lett.* **1998**, *441*, 11−14.

(14) Cotelesage, J. J. H.; Pushie, M. J.; Vogt, L.; Barney, M.; Nissan, A.; Pickering, I. J.; George, G. N. Insights into the Nature of the Chemical Bonding in Thiophene-2-thiol from X-ray Absorption Spectroscopy. *J. Phys. Chem. A* **2016**, *120*, 6929−6933.

(15) Pickering, I. J.; Barney, M.; Cotelesage, J. J. H.; Vogt, L.; Pushie, M. J.; Nissan, A.; Prince, R. C.; George, G. N. Chemical Sensitivity of the Sulfur K-Edge X-ray Absorption Spectra of Organic Disulfides. *J. Phys. Chem. A* **2016**, *120*, 7279−7286.

(16) Pushie, M. J.; Cotelesage, J. J. H.; Vogt, L.; Barney, M.; Pickering, I. J.; George, G. N.; George, G. N. Comment on "Insights into the Nature of the Chemical Bonding in Thiophene-2-thiol from X-ray Absorption Spectroscopy. *J. Phys. Chem. A* **2018**, *122*, 3711−3712.

(17) Martin-Diaconescu, V.; Kennepohl, P. Sulfur K-Edge XAS as a Probe of Sulfur-Centered Radical Intermediates. *J. Am. Chem. Soc.* **2007**, *129*, 3034−3035.

(18) Martin-Diaconescu, V.; Kennepohl, P. Effects of Hyperconjugation on the Electronic Structure and Photoreactivity of Organic Sulfonyl Chlorides. *Inorg. Chem.* **2009**, *48*, 1038−1044.

(19) Karunakaran-Datt, A.; Kennepohl, P. Redox Photochemistry of Methionine by Sulfur K-edge X-ray Absorption Spectroscopy: Potential Implications for Cataract Formation. *J. Am. Chem. Soc.* **2009**, *131*, 3577−3582.

(20) Martin-Diaconescu, V.; Perepichka, I.; Bohle, D. S.; Kennepohl, P. Electronic structure of S-nitrosothiols from sulfur K-edge X-ray absorption spectroscopy. *Can. J. Chem.* **2011**, *89*, 93−97.

(21) Sriskandakumar, T.; Behyan, S.; Habtemariam, A.; Sadler, P. J.; Kennepohl, P. Electrophilic Activation of Oxidized Sulfur Ligands and Implications for the Biological Activity of Ruthenium(II) Arene Anticancer Complexes. *Inorg. Chem.* **2015**, *54*, 11574−11580.

(22) Transue, W. J.; Nava, M.; Terban, M. W.; Yang, J.; Greenberg, M. W.; Wu, G.; Foreman, E. S.; Mustoe, C. L.; Kennepohl, P.; Owen,

J. S.; Billinge, S. J. L.; Kulik, H. J.; Cummins, C. C. Anthracene as a Launchpad for a Phosphinidene Sulfide and for Generation of a Phosphorus−Sulfur Material Having the Composition P_2S, a Vulcanized Red Phosphorus That Is Yellow. *J. Am. Chem. Soc.* **2019**, *141*, 431−440.
(23) Okbinoglu, T.; Kennepohl, P. Nature of S−N Bonding in Sulfonamides and Related Compounds: Insights into π-Bonding Contributions from Sulfur K-Edge X-ray Absorption Spectroscopy. *J. Phys. Chem. A* **2021**, *125*, 615−620.
(24) Szilagyi, R. K.; Frank, P.; DeBeer George, S.; Hedman, B.; Hodgson, K. O. High Covalence in $CuSO_4$ and the Radicalization of Sulfate: An X-ray Absorption and Density Functional Study. *Inorg. Chem.* **2004**, *43*, 8318−8329.
(25) Frank, P.; George, S. D.; Anxolabéhère-Mallart, E.; Hedman, B.; Hodgson, K. O. A Systematic Resolution of Sulfur in Reticulated Vitreous Carbon Using X-ray Absorption Spectroscopy. *Inorg. Chem.* **2006**, *45*, 9864−9876.
(26) Daly, S. R.; Keith, J. M.; Batista, E. R.; Boland, K. S.; Clark, D. L.; Kozimor, S. A.; Martin, R. L. Sulfur K-edge X-ray Absorption Spectroscopy and Time-Dependent Density Functional Theory of Dithiophosphinate Extractants: Minor Actinide Selectivity and Electronic Structure Correlations. *J. Am. Chem. Soc.* **2012**, *134*, 14408−14422.
(27) Behyan, S.; Hu, Y.; Urquhart, S. G. Sulfur 1s Near-Edge X-Ray Absorption Fine Structure (NEXAFS) of Thiol and Thioether Compounds. *J. Chem. Phys.* **2011**, *134*, 244304.
(28) Behyan, S.; Hu, Y.; Urquhart, S. G. Sulfur 1s Near Edge X-ray Absorption Fine Structure Spectroscopy of Thiophenic and Aromatic Thioether Compounds. *J. Chem. Phys.* **2013**, *138*, 214302.
(29) Pangamol, P.; Sirisinha, C.; Hu, Y. F.; Urquhart, S. G. Effectiveness of By-product Sulfur from Petroleum Refining as a Rubber Vulcanizing Agent: A XANES Investigation. *Ind. Eng. Chem. Res.* **2013**, *52*, 17179−17183.
(30) Behyan, S.; Hu, Y.; Urquhart, S. G. Chemical Sensitivity of Sulfur 1s NEXAFS Spectroscopy I: Speciation of Sulfoxides and Sulfones. *Chem. Phys. Lett.* **2014**, *592*, 69−74.
(31) Behyan, S.; Hu, Y.; Urquhart, S. G. Chemical Sensitivity of Sulfur 1s NEXAFS Spectroscopy II: Speciation of Disulfide Functional Groups. *Chem. Phys. Lett.* **2014**, *592*, 109−113.
(32) Küper, G.; Chauvistré, R.; Hormes, J.; Frick, F.; Jansen, M.; Lüer, B.; Hartmann, E. Phosphorus K shell photoabsorption spectra of the oxides P_4O_6, P_4O_{10}, $P(C_6H_5O)_3$ and $PO(C_6H_5O)_3$. *Chem. Phys.* **1992**, *165*, 405−414.
(33) Redeker, A.; Küper, G.; Hormes, J.; Frick, F.; Jansen, M.; Mühlhauser, M. Investigation of P_4O_6, P_4O_{10} and P_4O_6S by X-Ray Absorption Spectroscopy at the Phosphorus K-Edge. *Phosphorus, Sulfur Silicon Relat. Elem.* **1993**, *76*, 239−242.
(34) Franke, R.; Hormes, J. The P K-near edge absorption spectra of phosphates. *Phy. B* **1995**, *216*, 85−95.
(35) Yin, Z.; Kasrai, M.; Bancroft, G. M.; Tan, K. H.; Feng, X. X-ray-absorption spectroscopic studies of sodium polyphosphate glasses. *Phys. Rev. B* **1995**, *51*, 742−750.
(36) Okude, N.; Nagoshi, M.; Noro, H.; Baba, Y.; Yamamoto, H.; Sasaki, T. A. P. S K-edge XANES of transition-metal phosphates and sulfates. *J. Electron Spectrosc. Relat. Phenom.* **1999**, *101*, 607−610.
(37) Hesterberg, D.; Zhou, W.; Hutchison, K. J.; Beauchemin, S.; Sayers, D. E. XAFS study of adsorbed and mineral forms of phosphate. *J. Synchrotron Radiat.* **1999**, *6*, 636−638.
(38) Ingall, E. D.; Brandes, J. A.; Diaz, J. M.; de Jonge, M. D.; Paterson, D.; McNulty, I.; Elliott, W. C.; Northrup, P. Phosphorus K-edge XANES spectroscopy of mineral standards. *J. Synchrotron Radiat.* **2011**, *18*, 189−197.
(39) Peak, D.; Sims, J. T.; Sparks, D. L. Solid-State Speciation of Natural and Alum-Amended Poultry Litter Using XANES Spectroscopy. *Environ. Sci. Technol.* **2002**, *36*, 4253−4261.
(40) Prietzel, J.; Thieme, J.; Paterson, D. Phosphorus speciation of forest-soil organic surface layers using P K-edge XANES spectroscopy. *J. Plant Nutr. Soil Sci.* **2010**, *173*, 805−807.
(41) Kar, G.; Hundal, L. S.; Schoenau, J. J.; Peak, D. Direct Chemical Speciation of P in Sequential Chemical Extraction Residues Using P K-Edge X-Ray Absorption Near-Edge Structure Spectroscopy. *Soil Sci.* **2011**, *176*, 589−595.
(42) Weyers, E.; Strawn, D. G.; Peak, D.; Baker, L. L. Inhibition of phosphorus sorption on calcite by dairy manure-sourced DOC. *Chemosphere* **2017**, *184*, 99−105.
(43) Engemann, C.; Franke, R.; Hormes, J.; Lauterbach, C.; Hartmann, E.; Clade, J.; Jansen, M. X-ray absorption near-edge spectroscopy (XANES) at the phosphorus K-edge of triorganophosphinechalcogenides. *Chem. Phys.* **1999**, *243*, 61−75.
(44) Donahue, C. M.; Daly, S. R. Ligand K-Edge XAS Studies of Metal-Phosphorus Bonds: Applications, Limitations, and Opportunities. *Comments Inorg. Chem.* **2018**, *38*, 54−78.
(45) Persson, I.; Klysubun, W.; Lundberg, D. A K-edge P XANES study of phosphorus compounds in solution. *J. Mol. Struct.* **2019**, *1179*, 608−611.
(46) Wibowo, R. E.; Garcia-Diez, R.; van der Merwe, M.; Duarte-Ruiz, D.; Ha, Y.; Félix, R.; Efimenko, A.; Bystron, T.; Prokop, M.; Wilks, R. G.; Bouzek, K.; Yang, W.; Cocchi, C.; Bär, M. Core-Level Spectroscopy with Hard and Soft X-Rays on Phosphorus-Containing Compounds for Energy Conversion and Storage. *J. Phys. Chem. C* **2023**, *127*, 20582−20593.
(47) Blake, A. V.; Wei, H.; Lee, K.; Donahue, C. M.; Keith, J. M.; Daly, S. R. Solution and Solid-State Ligand K-Edge XAS Studies of $PdCl_2$ Diphosphine Complexes with Phenyl and Cyclohexyl Substituents. *Eur. J. Inorg. Chem.* **2018**, *2018*, 2267−2276.
(48) Lee, K.; Wei, H.; Blake, A. V.; Donahue, C. M.; Keith, J. M.; Daly, S. R. Measurement of Diphosphine σ-Donor and π-Acceptor Properties in d^0 Titanium Complexes Using Ligand K-Edge XAS and TDDFT. *Inorg. Chem.* **2018**, *57*, 10277−10286.
(49) Blake, A. V.; Wei, H.; Donahue, C. M.; Lee, K.; Keith, J. M.; Daly, S. R. Solid energy calibration standards for P K-edge XANES: electronic structure analysis of PPh_4Br. *J. Synchrotron Radiat.* **2018**, *25*, 529−536.
(50) Lee, K.; Blake, A. V.; Donahue, C. M.; Spielvogel, K. D.; Bellott, B. J.; Daly, S. R. Quantifying the Interdependence of Metal−Ligand Covalency and Bond Distance Using Ligand K-edge XAS. *Angew. Chem., Int. Ed.* **2019**, *58*, 12451−12455.
(51) Lee, K.; Blake, A. V.; Tanushi, A.; McCarthy, S. M.; Kim, D.; Loria, S. M.; Donahue, C. M.; Spielvogel, K. D.; Keith, J. M.; Daly, S. R.; Radosevich, A. T. Validating the Biphilic Hypothesis of Nontrigonal Phosphorus(III) Compounds. *Angew. Chem., Int. Ed.* **2019**, *58*, 6993−6998.
(52) Herzberg, G. *Molecular Spectra & Molecular Structure, Vol I − Spectra of Diatomic Molecules*, 2nd ed. ed.; Krieger Publishing: Malabar Florida, 1989; p 383.
(53) Küper, G.; Hormes, J.; Sommer, K. In situ X-ray absorption spectroscopy at the K-edge of red phosphorus in polyamide 6,6 during a thermo-oxidative degradation. *Macromol. Chem. Phys.* **1994**, *195*, 1741.
(54) Jayaraman, A.; Sterenberg, B. T. Phosphorus−Carbon Bond Forming Reactions of Diphenylphosphenium and Diphenylphosphine Triflate Complexes of Tungsten. *Organometallics* **2016**, *35*, 2367−2377.
(55) Borst, M. L. G.; Bulo, R. E.; Gibney, D. J.; Alem, Y.; de Kanter, F. J. J.; Ehlers, A. W.; Schakel, M.; Lutz, M.; Spek, A. L.; Lammertsma, K. 3*H*-Benzophosphepine Complexes: Versatile Phosphinidene Precursors. *J. Am. Chem. Soc.* **2005**, *127*, 16985−16999.
(56) Jayaraman, A.; Jacob, T. V.; Bisskey, J.; Sterenberg, B. T. Sequential electrophilic P−C bond formation in metal-coordinated chlorophosphines. *Dalton Trans.* **2015**, *44*, 8788−8791.
(57) Jayaraman, A.; Nilewar, S.; Jacob, T. V.; Sterenberg, B. T. Sequential Electrophilic Substitution Reactions of Tungsten-Coordinated Phosphenium Ions and Phosphine Triflates. *ACS Omega* **2017**, *2*, 7849−7861.
(58) Frisch, M. J.; Trucks, G. W.; Schlegel, H. B.; Scuseria, G. E.; Robb, M. A.; Cheeseman, J. R.; Scalmani, G.; Barone, V.; Petersson, G. A.; Nakatsuji, H.; Li, X.; Caricato, M.; Marenich, A.; Bloino, J.;

https://doi.org/10.1021/acs.jpcc.4c03887
J. Phys. Chem. C 2024, 128, 14750−14760

Janesko, B. G.; Gomperts, R.; Mennucci, B.; Hratchian, H. P.; Ortiz, J. V.; Izmaylov, A. F.; Sonnenberg, J. L.; Williams-Young, D.; Ding, F.; Lipparini, F.; Egidi, F.; Goings, J.; Peng, B.; Petrone, A.; Henderson, T.; Ranasinghe, D.; Zakrzewski, V. G.; Gao, J.; Rega, N.; Zheng, G.; Liang, W.; Hada, M.; Ehara, M.; Toyota, K.; Fukuda, R.; Hasegawa, J.; Ishida, M.; Nakajima, T.; Honda, Y.; Kitao, O.; Nakai, H.; Vreven, T.; Throssell, K.; Montgomery, J. A.; Peralta, J. E.; Ogliaro, F.; Bearpark, M.; Heyd, J. J.; Brothers, E.; Kudin, K. N.; Staroverov, V. N.; Keith, T.; Kobayashi, R.; Normand, J.; Raghavachari, K.; Rendell, A.; Burant, J. C.; Iyengar, S. S.; Tomasi, J.; Cossi, M.; Millam, J. M.; Klene, M.; Adamo, C.; Cammi, R.; Ochterski, J. W.; Martin, R. L.; Morokuma, K.; Farkas, O.; Foresman, J. B.; Fox, D. J. *Gaussian 16*. Revision C.01; Gaussian, Inc.: Wallingford CT, 2016;

(59) Casida, M. E. Time-Dependent Density-Functional Response Theory for Molecules. In *Recent Advances in Density Functional Methods, Part I*; Chong, D. P., Ed.; World Scientific: Singapore, 1995; pp 155−192.

(60) Casida, M. E.; Huix-Rotllant, M. Progress in Time-Dependent Density-Functional Theory. *Annu. Rev. Phys. Chem.* **2012**, *63*, 287−323.

(61) Hirata, S.; Head-Gordon, M. Time-dependent density functional theory within the Tamm-Dancoff approximation. *Chem. Phys. Lett.* **1999**, *314*, 291−299.

(62) Neese, F. Software update: The ORCA program system − Version 5.0. *Wiley Interdiscip. Rev. Comput. Mol. Sci.* **2022**, *12*, No. e1606.

(63) Becke, A. D. A new mixing of Hartree-Fock and local density-functional theories. *J. Chem. Phys.* **1993**, *98*, 1372−1377.

(64) Lee, C.; Yang, W.; Parr, R. G. Development of the Colle-Salvetti Correlation Energy Formula into a Functional of the Electron Density. *Phys. Rev. B: Condens. Matter Mater. Phys.* **1988**, *37*, 785−789.

(65) Dunning, T. H., Jr Gaussian basis sets for use in correlated molecular calculations. I. The atoms boron through neon and hydrogen. *J. Chem. Phys.* **1989**, *90*, 1007−1023.

(66) Woon, D. E.; Dunning, T. H., Jr Gaussian basis sets for use in correlated molecular calculations. III. The atoms aluminum through argon. *J. Chem. Phys.* **1993**, *98*, 1358−1371.

(67) Balabanov, N. B.; Peterson, K. A. Systematically convergent basis sets for transition metals. I. All-electron correlation consistent basis sets for the 3d elements Sc−Zn. *J. Chem. Phys.* **2005**, *123*, 064107.

(68) Van Wullen, C. Molecular density functional calculations in the regular relativistic approximation: Method, application to coinage metal diatomics, hydrides, fluorides and chlorides, and comparison with first-order relativistic calculations. *J. Chem. Phys.* **1998**, *109*, 392−399.

(69) Neese, F.; Wennmohs, F.; Hansen, A.; Becker, U. Efficient, approximate and parallel Hartree−Fock and hybrid DFT calculations. A 'chain-of-spheres' algorithm for the Hartree−Fock exchange. *Chem. Phys.* **2009**, *356*, 98−109.

(70) Pantazis, D. A.; Chen, X.-Y.; Landis, C. R.; Neese, F. All-Electron Scalar Relativistic Basis Sets for Third-Row Transition Metal Atoms. *J. Chem. Theory Comput.* **2008**, *4*, 908−919.

(71) DeBeer George, S.; Petrenko, T.; Neese, F. Time-dependent density functional calculations of ligand K-edge X-ray absorption spectra. *Inorg. Chim. Acta* **2008**, *361*, 965−972.

(72) Hanwell, M. D.; Curtis, D. E.; Lonie, D. C.; Vandermeersch, T.; Zurek, E.; Hutchison, G. R. Avogadro: An advanced semantic chemical editor, visualization, and analysis platform. *J. Cheminf.* **2012**, *4*, 17.

(73) Mathe, Z.; McCubbin Stepanic, O.; Peredkov, S.; DeBeer, S. Phosphorus Kβ X-ray emission spectroscopy detects non-covalent interactions of phosphate biomolecules *in situ*. *Chem. Sci.* **2021**, *12*, 7888−7901.

(74) Dalba, G.; Fornasini, P.; Rocca, F.; Lagarde, P.; Vlaic, G. EXAFS Study of the Coordination of Phosphorus in $AgPO_3$ Glass. *J. Non-Cryst. Solids* **1988**, *106*, 181−184.

(75) Persson, I.; Trublet, M.; Klysubun, W. Structure Determination of Phosphoric Acid and Phosphate Ions in Aqueous Solution Using EXAFS Spectroscopy and Large Angle X-ray Scattering. *J. Phys. Chem. A* **2018**, *122*, 7413−7420.

(76) Fano, U.; Cooper, J. W. Line Profiles in the Far-uv Absorption Spectra of the Rare Gases. *Phys. Rev.* **1965**, *137*, A1364−A1379.

(77) Francis, J. T.; Hitchcock, A. P. Inner-Shell Spectroscopy of p-Benzoquinone, Hydroquinone, and Phenol: Distinguishing Quinoid and Benzenoid Structures. *J. Phys. Chem.* **1992**, *96*, 6598−6610.

(78) Leetmaa, M.; Ljungberg, M. P.; Lyubartsev, A.; Nilsson, A.; Pettersson, L. G. M. Theoretical approximations to X-ray absorption spectroscopy of liquid water and ice. *J. Electron Spectrosc. Relat. Phenom.* **2010**, *177*, 135−157.

(79) Fano, U.; Cooper, J. W. Spectral Distribution of Atomic Oscillator Strengths. *Rev. Mod. Phys.* **1968**, *40*, 441−507.

(80) Sette, F.; Stöhr, J.; Hitchcock, A. P. Determination of intramolecular bond lengths in gas phase molecules form K shell shape resonances. *J. Chem. Phys.* **1984**, *81*, 4906−4914.

(81) Reed, A. E.; Weinstock, R. B.; Weinhold, F. Natural population analysis. *J. Chem. Phys.* **1985**, *83*, 735−746.

(82) Allred, A. L. Electronegativity Values from Thermochemical Data. *J. Inorg. Nucl. Chem.* **1961**, *17*, 215−221.

(83) Allen, L. C. Electronegativity Is the Average One-Electron Energy of the Valence-Shell Electrons in Ground-State Free Atoms. *J. Am. Chem. Soc.* **1989**, *111*, 9003−9014.

https://doi.org/10.1021/acs.jpcc.4c03887
J. Phys. Chem. C 2024, 128, 14750−14760